**RESEARCH**                                                                                    **Open Access**

# High-Strength Reinforcing Steel Bars: Low Cycle Fatigue Behavior Using RGB Methodology

Jorge E. Egger⬛, Fabian R. Rojas*⬛ and Leonardo M. Massone⬛

## Abstract

Low cycle fatigue life of high-strength reinforcing steel bars (ASTM A706 Grade 80), using photogrammetry by RGB methodology is evaluated. Fatigue tests are performed on specimens under constant axial displacement with total strain amplitudes ranging from 0.01 to 0.05. The experimental observations indicate that buckling of high-strength reinforcing bars results in a damaging degradation of their fatigue life performance as the slenderness ratio increases, including an early rebar failure as the total strain amplitude increases since it achieves the plastic range faster. In addition to this, the results show that the ratio of the ultimate tensile strength to yield strength satisfies the mini-mum of 1.25 specified in ASTM A706 for reinforcement. On the other hand, the RGB methodology indicates that the axial strains measured by photogrammetry provide more accurate data since the registered results by the traditional experimental setup do not detect second-order effects, such as slippage or lengthening of the specimens within the clamps. Moreover, the RGB filter is faster than digital image correlation (DIC) because the RGB methodology requires a fewer computational cost than DIC algorithms. The RGB methodology allows to reduce the total strain amplitude up to 45% compared to the results obtained by the traditional setup. Finally, models relating total strain amplitude with half-cycles to failure and total strain amplitude with total energy dissipated for multiple slenderness ratios (*L/d* of 5, 10, and 15) are obtained.

**Keywords:** fatigue life, high-strength steel, hysteresis, photogrammetry, reinforcing bars, RGB filter

## 1 Introduction

The use of high-strength materials such as concrete and steel has recently received attention in Chile due to the demand for large scale new structures, as the Chacao Channel bridge with a total length of 2.75 km. It is impor-tant to consider that the highest value in the formation of a new artificial habitat is placed on architecture and con-struction, as well as on the applied materials, and the new artificial environments should ensure a positive impact on psycho-emotional and physical conditions (Elistrat-kin et al. 2018). By using high-strength concrete and steel in large structures, the structural element section size and reinforcement agglomeration can be reduced. For example, large structures, as high-rise buildings, involve more floor area, which can be achieved by designing the size of lower-story columns using materials with higher strength. Current US bridge code provisions does not allow high-strength steel in structural components des-ignated as part of the seismic-force-resisting system (AASHTO 2017). Despite this, Chile recently adopted a new code (NCh 204: 2020) based on ACI 318-19 (2019), which is expected to produce an immense variety of pro-gressively more slender buildings essentially based on the US reinforced concrete code. Moreover, it includes two new grades of steel: A700H and A730H, which allow Chilean structural engineering to take a better advantage of the use of steel, especially in larger works, and to con-sider the behavior under cyclic loads.

On the other hand, low cycle fatigue behavior is described as a untimely fracture of reinforcing bar under constant or variable strain amplitude cyclic loading with

*Correspondence: fabianrojas@uchile.cl
Department of Civil Engineering, University of Chile, Blanco Encalada 2002, Santiago, Chile

Egger *et al. Int J Concr Struct Mater*    (2021) 15:38

Page 2 of 13

a respective low value of cycles (less than 1000). The fatigue damage accumulation in the reinforcement happens over the life span of the structural element (during earthquakes), and arguably may cost in premature failure of the reinforcement. In reinforced concrete structures (RC) designed to generally react in flexure under an earthquake, their fracture is especially related to failure of reinforcement due to buckling in cases with inadequate lateral restraint given by the transverse reinforcing bars. In most of the flexural damage options described, buckling of reinforcement is possibly the most usual failure option that has been reported in the $M_w$ 8.8 earthquake in Chile on February 27, 2010 (Carpenter et al. 2011; Naeim et al. 2011; Rojas et al. 2010, 2011).

Experimental investigations were conducted by Brown and Kunnath (2004) on ASTM A615 with multiple diameters to understand the fatigue failure of reinforcing bars. Fatigue models were presented using the total and plastic strain amplitude, and total energy dissipated. Barbosa et al. (2017) performed reversed fatigue loading on ASTM A615 and ASTM A706 at Grade 60 and Grade 80, and compared toughness fatigue life predictions. Tripathi et al. (2018) performed a set of experiments on similar rebars, on Grade 300E and 500E, subjected to cyclic tests with axial strains up to 0.05 and including the effect of inelastic buckling. Sokoli et al. (2019), based on the work of Ghannoum and Slavin (2016), performed fatigue tests on Grade 60, 80 and 100 bars to understand the fatigue failure of reinforcement in plastic hinge locations, and derived that fatigue life of reinforcement with close yield strengths for multiple bar species may be considerably diverse. These models are considered as referential in this work for theoretical purposes. Although it has been accepted that buckling of reinforcement exhibits a drop of the fatigue performance due to the weakening of the specimen at the critical region, few information has been discussed in the literature on the effect of ductility of high-strength rebars or even the strain penetration on fatigue behavior of reinforcing steel in an experimental measurement. Additionally, the effect factors on the fatigue life of high-strength steel in RC structures generate many complications when considering natural phenomena, such as the stress produced by seismic events or the deterioration caused by corrosive environments, accelerating the damage and impacting the mechanical properties of the steel (Hu et al. 2019; Wang et al. 2021). In addition to this, when fatigue loading is not applied at a constant harmonic amplitude, it is important to consider the cumulative fatigue damage, known as the Palmgren–Miner rule (Fisher et al. 1998) , which assumes that the damage fraction that results from any particular stress range level is a linear function of the number of cycles that takes place at the stress range. It is important

to contemplate this rule because the US bridge code advises it to account for cumulative damage (AASHTO 2017). Considering the previous discussion, this article emphasizes in representing the behavior of high-strength reinforcement in an environment of optimal conditions under constant cyclic loading, similar to the strain ranges and geometries produced by seismic loads in the natural field based on the results observed in the 2010 Chile earthquake (Massone 2013; Wallace et al. 2012).

In this study, photogrammetry using RGB methodology performed in MATLAB (2018) is also applied, providing greater data accuracy compared to the total strain amplitude obtained by the traditional experimental setup. Photogrammetry is the technique whose object is to study and precisely define the shape, dimensions and position in space of any object, essentially using measurements made on one or more consecutive photographs of that object. In this case, the incorporation of a high-resolution camera allows to directly determine the axial strains of the specimen in 2D during the tests. Photogrammetry is complementary to the traditional experimental setup, and allows correcting the data obtained. Accuracy is highly important to evaluate fatigue life models correctly, and photogrammetry can be used to obtain data that traditional experimental setup cannot register, as slippage of reinforcing bars or plastic strain lengthening within the clamps. A significant number of articles use programs based on digital image correlation (DIC) to measure strains, such as NCorr (Blaber et al. 2015), 2D DIC (Pan et al. 2009), or UTVS (Sokoli et al. 2014), which are based on tracking target locations in each recorded frame using a DIC algorithm. Nevertheless, the processing time of a photo with DIC is much longer than the time used by RGB methodology due to the algorithms that DIC uses to iterate, track and correlate each pixel has a high computational cost, which means that the filtering time for each photograph is longer. Therefore, this article investigates the impact of low cycle fatigue behavior of high-strength reinforcing bars, differing from other articles by applying RGB filter. The main purposes are four important topics: (i) to analyze and investigate the behavior of Grade 80 reinforcing bars under reverse and symmetric strain amplitude cyclic loading; (ii) to use RGB methodology to improve the accuracy of experimental data; (iii) to analyze the impact of buckling on fatigue performance of high-strength reinforcement; and (iv) to calibrate fatigue life models using the experimental results obtained by RGB filter.
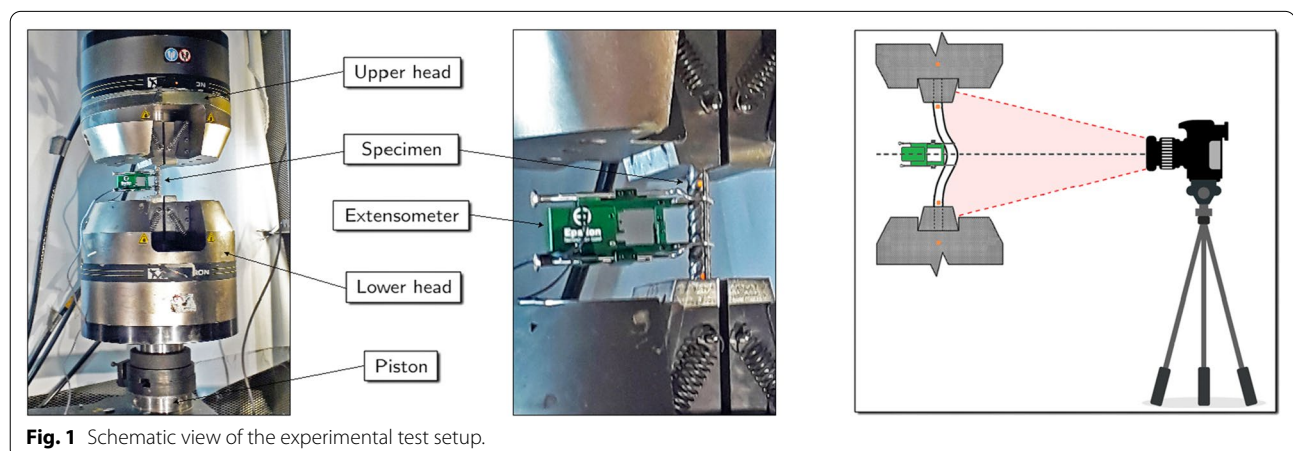
## 2 Experimental Procedure, Analysis and Results
In this work, ASTM A706 Grade 80 reinforcing bars are tested by subjecting to a cycling displacement pattern in order to get their low cycle fatigue life. A schematic view

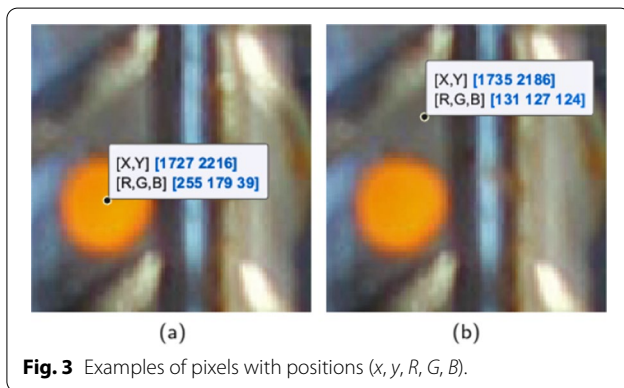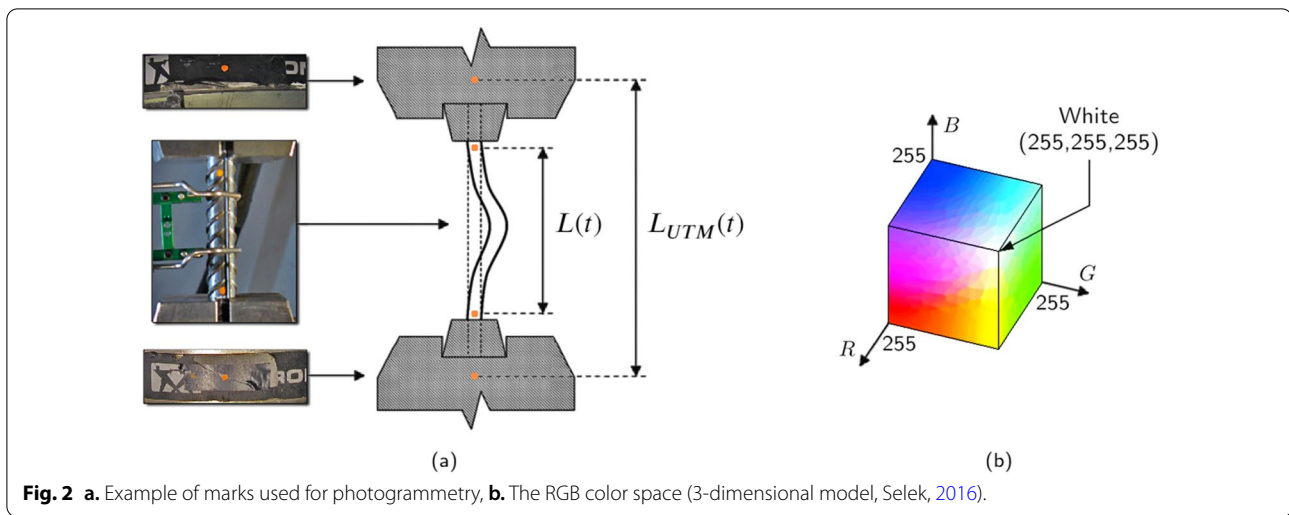Egger *et al. Int J Concr Struct Mater*     (2021) 15:38

Page 3 of 13

of the test setup and instrumentation used in the Department of Civil Engineering at the University of Chile for the monotonic tensile and cyclic tests is shown in Fig. 1. Monotonic uniaxial tensile test and fatigue tests are performed on 12-mm-diameter ($\phi$12) rebars using a universal testing machine (UTM) model INSTRON 600 LX, as shown in Fig. 1, recording the force and displacement. A high-resolution camera positioned frontally to the test specimen is used, in order to take photographs during the experimental test, which are subsequently processed by photogrammetry to obtain the displacements over time of color marks applied on the specimen as in the UTM. This methodology allows describing the position of the center of each mark over time, where each photograph of 3456x5184 recorded during the test (each 5 s using DSLR Remote Pro Multi-Camera DSLR Remote Pro (2017)) can be filtered through ranges of specific colors. The image filtering will be explained in more detail later. An extensometer, with a gauge length of 25 mm, is mounted at the middle of the length of reinforcing bar to measure the axial strains (initial elastic behavior) until the test achieves yield stress. The objective of using an extensometer is to compare the results of the initial elastic response of the high-strength steel with the correction obtained initially by photogrammetry. It is important to remove the extensometer from the specimen at this point as failure of the rebar can damage the instrument. The referential monotonic tensile test is performed on a specimen with a total length of 300 mm (i.e., the length of the reinforcing bar without the gripping length of 75 mm) and the axial strains are measured by photogrammetry at the effective length of the reinforcing bar within a gauge length of 150 mm. The stresses are obtained through the ratio of applied load over the initial cross-sectional area of the specimen, and for each cyclic test, steel bars are cut based on the specific slenderness ratios $L/d$ (relationship between buckling length $L$ and the diameter $d$) to ensure that the specimen is tightened by the clamps. Additionally, the cyclic tests are subjected using a custom displacement control.

## 2.1 Photogrammetry Using RGB Methodology

Measurement techniques have improved over the years to encompass more data information as accurate as possible. One of these techniques is known as photogrammetry, which has been developed in multiple areas of engineering. The importance of photogrammetry in tensile tests or low cycle fatigue tests is to measure axial strains of the specimen as accurate as possible, since traditional equipment is unable to detect secondary effects, such as the possible plastic lengthening of the bar within the clamps (known as strain penetration, Massone and Herrera 2019), or slippage of the bar inside the clamps. This effect originates mainly from the imperfect embedment at the clamp–bar system, where due to the presence of axial load the specimen experiences a decrease in its cross-sectional area, facilitating deformations in the zone in contact with the clamp. In this study, RGB filter is used (López 2019). The RGB color space consists of three main color components; namely, R, G and B (Selek 2016), which are based on the intensity of the primary colors of light: red, green and blue, respectively. It is a chromatic model through which different broad array of colors can be reproduced from RGB mixture. The basic element used in an image is the pixel, which is expressed in an image as a certain color using RGB or grayscale definition. This methodology allows describing the position of a pixel over time, where each photograph recorded during the test can be filtered through ranges of specific RGB colors. Orange marks are applied in Fig. 2a on the upper head and lower head, respectively (to verify and check the axial strains obtained by the UTM and



**Fig. 1** Schematic view of the experimental test setup.

**Fig. 2** **a.** Example of marks used for photogrammetry, **b.** The RGB color space (3-dimensional model, Selek, 2016).



**Fig. 3** Examples of pixels with positions (*x, y, R, G, B*).

by photogrammetry using $L_{UTM}(t)$), and orange marks on the bar near the clamps (to obtain the axial strains of the reinforcement with greater accuracy using $L(t)$). The purpose of placing marks close to the clamps is to track the pixels of these marks over time to calculate the overall longitudinal strain along the clear span. It is possible to represent in MATLAB each pixel pointing its position (*x, y*) and including its color position (*R, G, B*) in the RGB color space as illustrated in Fig. 2b. This 5-dimensional space can be observed using the function *imshow*() as shown in Fig. 3. The following RGB ranges present the filters used in the example in Fig. 3 are: $200 \leq R \leq 255$, $120 \leq G \leq 190$, and $20 \leq B \leq 80$.

Focusing on *B* coordinate, Fig. 3a shows that *B* is between the values 20 and 80 if the pixel is within the orange mark (*B* coordinate is 39), while if the position of any pixel outside the orange mark is observed as Fig. 3b, *B* coordinate is no longer within the range of values 20 and 80 (*B* coordinate is 124), so the pixel out of range is discarded by the RGB filter. Depending on the test, the RGB ranges can be modified based on the coordinates observed in the first

photograph at the beginning of the test. The purpose is that the filter provides the best representation of the orange (or another color) marks. Then, a binary matrix composed of 0 (if the pixel is outside the RGB ranges) and 1 (if the pixel is within the RGB ranges) is created. To observe the filtered image, as the one in Fig. 4, the MATLAB function *spy*(*b*) can be used, where *b* is the binary matrix. Once the filter has been applied, the position of the center of each orange mark can be followed over time (represented in Fig. 4 as a yellow point). For this, the range of analysis in (*x, y*) must be defined for each mark, in order to obtain the precise position of the center of the orange mark for the upper and the lower points. Fig. 4 illustrates the upper coordinate point $(px_1, py_1)$ and the lower coordinate point $(px_2, py_2)$ in an instant of time. The upper point is exemplified with a range of analysis for *x* of $\pm 30$ pixels, and with a range of analysis for *y* of $\pm 60$ pixels. Using this information, and also considering an initial iteration position proposed by the user (preferably the center of the orange mark), an average is calculated between the coordinates of all pixels equal to 1 (both for *x* and for *y* separately) and thus the initial coordinate $(px_1(t_1), py_1(t_1))$ is obtained. Then, this same coordinate is used as the starting point of the iteration, and the following coordinate $(px_1(t_2), py_1(t_2))$ is obtained, continuing with the same approach successively for different photographs over time. Finally, the axial strain as a function of time *t*, with initial time $t_1 = 0$ sec., is obtained in Eq. 2:

$$L(t) = py_2(t) - py_1(t), \tag{1}$$

$$\epsilon_{RGB}(t) = \frac{L(t) - L(t_1)}{L(t_1)}, \tag{2}$$

where $L(t)$ is the relative buckling length over time obtained by photogrammetry, and $\epsilon_{RGB}(t)$ is the axial strain as a function of time obtained by RGB
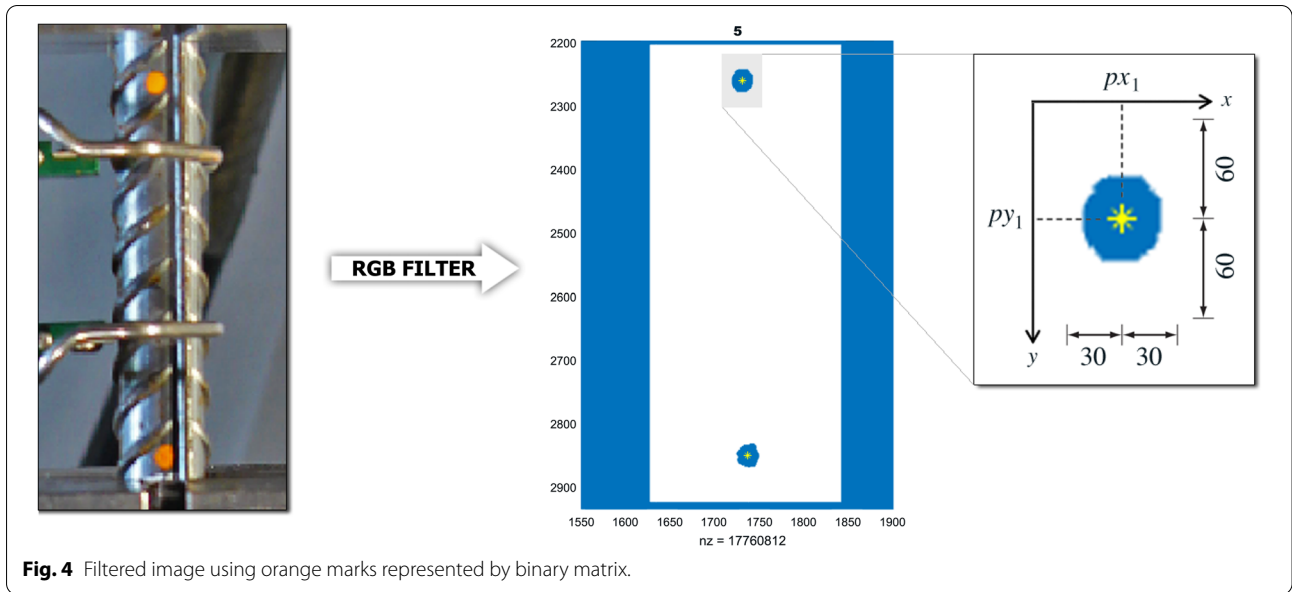
**Fig. 4** Filtered image using orange marks represented by binary matrix.

methodology. It should be mentioned that it is not necessary to describe the pixel ratio per unit length in these equations, since the axial strain $\epsilon_{RGB}$ is dimensionless. As the vector $\epsilon_{RGB}(t)$ obtained by RGB methodology does not have the same length as $\epsilon_{UTM}(t)$ registered by the experimental setup, it is recommended to generate an algorithm that records the maximum and minimum strain values of $\epsilon_{RGB}(t)$ for each cycle, and then each value of the respective cycle for $\epsilon_{UTM}(t)$ is reduced by a lineal percentage using the strain peaks recorded and obtained by photogrammetry. The purpose of having the same vector lengths is to generate the hysteresis curves using the stress registered by the UTM.

## 2.2 Compatibility Conditions for Deformations

The work by Yang et al. (2016) describes the transverse displacement of buckling bars as a function of axial displacement, as shown in Eq. 3:

$$w(t) = \sqrt{\delta(t) \cdot (L(0) - 2l_p)/2}, \tag{3}$$

where $w(t)$ is the transverse displacement of buckling bars over time, $\delta(t)$ is the axial displacement as a function of time, and $l_p$ is a parameter obtained from the geometry of the specimen. However, it assumes that the embedment at the clamps is perfect and no rotations or displacements are possible, which is not the case in the experimental tests using photogrammetry as shown in Fig. 5. Therefore, is very important to check deformation compatibility as shown in Fig. 6, where $\epsilon(t) = \delta(t)/L(0)$. As previously discussed, during testing there exists secondary effects in the specimen, such as strain penetration
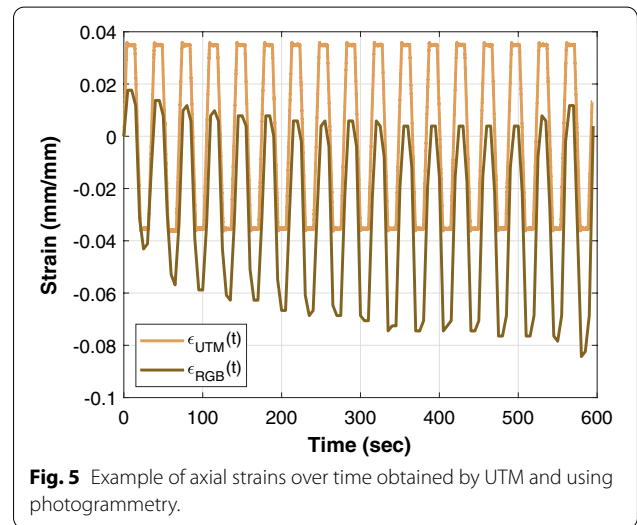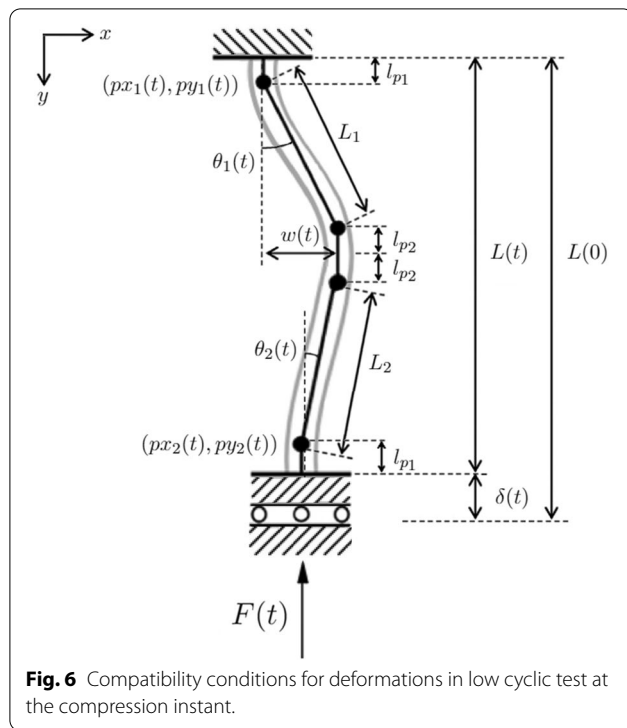


**Fig. 5** Example of axial strains over time obtained by UTM and using photogrammetry.

(possible plastic lengthening or elongation of the bar inside the clamps), and also rotation caused by the moment at the embedment of the bar at the clamps ($\theta_1$, $\theta_2$), translated as a horizontal displacement. This effect occurs because $px_1$ and $px_2$ coordinates constantly oscillate over time. A particular event occurs when buckling length is less or equal than $5d$. In this case, the axial force $F(t)$ produced by the UTM and the difference between both horizontal coordinates, cause an horizontal movement in the clamps bigger than cases with buckling length larger than $5d$. According to the geometry, the inclined straight spaces $L_1, L_2$ have a length of $L/2 - l_p$, and the plastic hinges have a constant length of

Egger *et al. Int J Concr Struct Mater* (2021) 15:38

Page 6 of 13



**Fig. 6** Compatibility conditions for deformations in low cyclic test at the compression instant.

$l_p = l_{p1} + l_{p2} \approx d$, such that the relative vertical displacement is determined as:

$$L(t) = L(0) - \frac{[px_2(t) - px_1(t) - w(t)]^2 + w(t)^2}{L(0) - 2l_p},$$
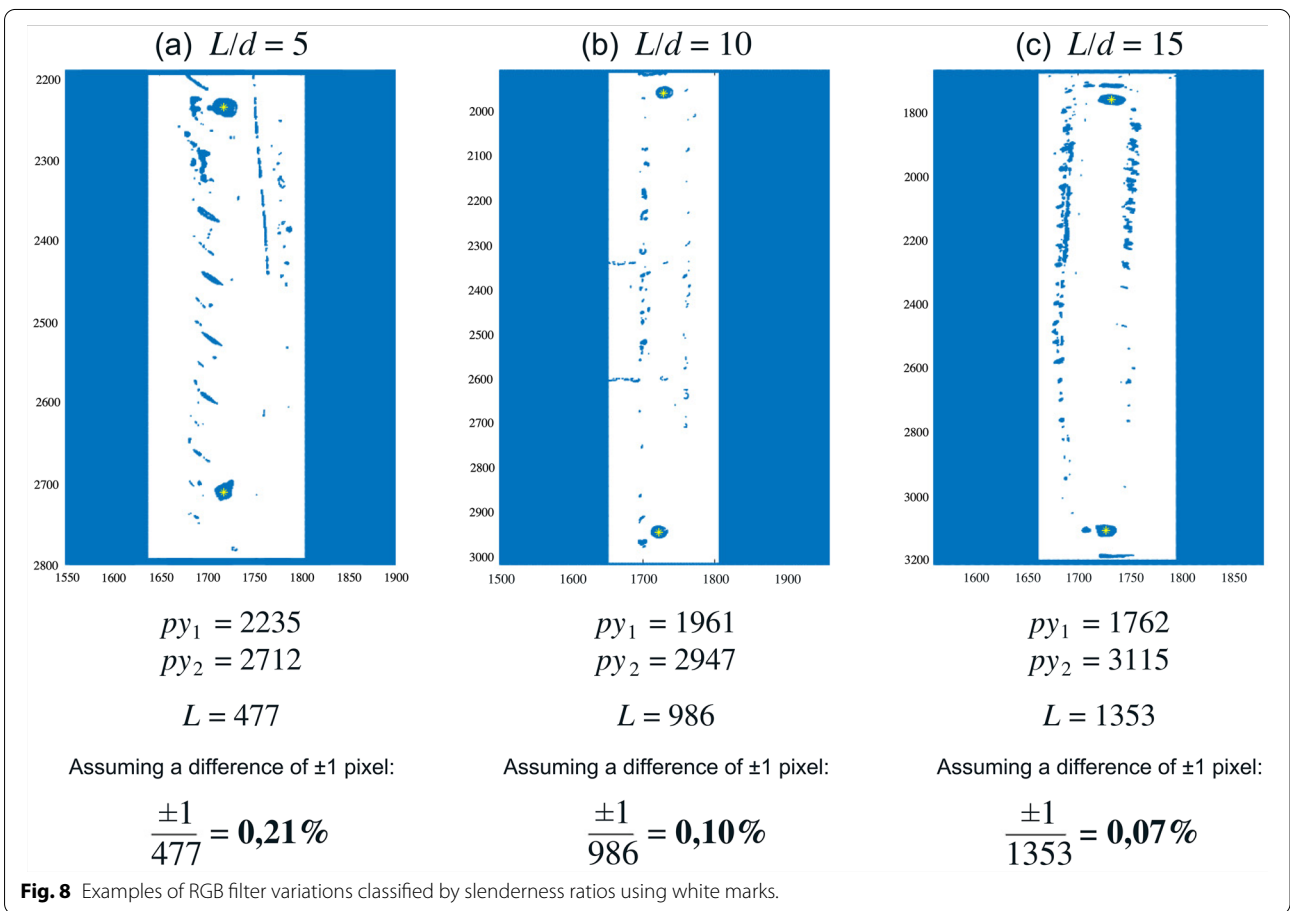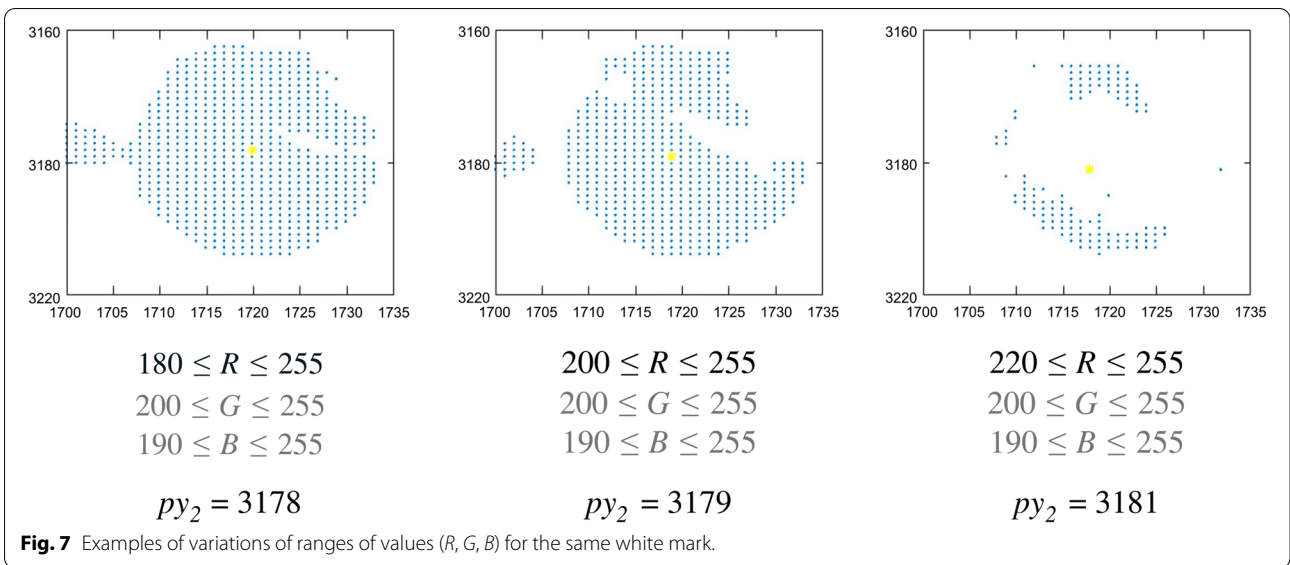(4)

Eq. 4 is obtained based exclusively on the criteria and approximations of Yang et al. (2016) such as using Taylor series to the functions $\sin(\theta)$ and $\cos(\theta)$, which allow to ignore terms with small distances and assume that $L(t)$ is the relative difference between $py_1(t)$ and $py_2(t)$ as shown in Eq. 1. On the other hand, Eq. 4 shows that the relative buckling length $L(t)$ is implicitly dependent on the horizontal positions $px_1$ and $px_2$. If there is a difference in $x$, an additional moment will be generated in the embedment produced by the axial force $F(t)$ and the axial strain in $y$ will be affected. Even if $px_1 = px_2$ in Eq. 4, Eq. 3 is obtained. In addition, $w(t)$ is not numerically relevant at the instant of compression ($w_{max}$) as it will discuss in the fatigue test results. All external trends can be ignored in MATLAB using the function *detrend*(), which can remove the nth-degree polynomial trend generated by the difference between $px_1$ and $px_2$. It is necessary to eliminate the trend since it is a second-order effect that affects the resulting hysteresis. It should be mentioned that this study only uses one camera for the $x$ and $y$ axes. This does not show the movements that may occur in the specimen on the $z$ axis, which can also affect the movement of the specimen and the clamps.

## 2.3 Accuracy and Sensitivity of Photogrammetry

The accuracy is directly related to the number of pixels available within a measurement, since the minimal distance that can be measured in an image is the distance between two pixels. This point means that if the scale is 5 mm/pixel, the minimal observed distance is 5 millimeters. This indicates that if the camera zooms in the steel bar, the deformations and displacements of the surface will be measured in more detail. There is also differences in the position of the mark associated with two consecutive photographs at rest without testing. By performing two RGB filters on both photographs, it can be observed that vibrations or disturbances in the laboratory may produce a variation of the center of the RGB-filtered mark. The interval at which the photographs are taken should be designed to capture strain peaks. For this work, a time interval of 5 seconds is optimal to obtain extreme values. However, these physical or environmental sensitivity issues are less relevant than other variations.

The first is related to the ranges of values for the coordinates ($R$, $G$, $B$) used for the filter of a photograph, so there may be issues when not considering the correct or precise ranges. Fig. 7 shows three examples of filter ranges for the same mark of white color, which had problems with the reflection of light on the surface of the rebar, and each example has constant ranges of $G$ and $B$, except for $R$. The average variation in this particular case is $\pm 1$ pixel, since the position of $py_2$ varies by 1 pixel on average when modifying the $R$ range and leaving the ranges $G$ and $B$ constant. To address this problem, it must observe in the filter if all useful pixels are being considered to determine the center of each mark. This sometimes leads to certain pixels not being considered for the final filter, as can be seen in Fig. 7. This implies that the ranges to be used in this methodology must cover and detect all useful pixels to avoid losing important information, as well the color of the mark must be consistent with the luminosity. The second common issue in this methodology is related to the measuring length, which in this case is associated to the resolution of the camera recording a shorter buckling length (or recording a fewer number of pixels). Fig. 8 shows three examples for multiple slenderness ratios: from left to right, $L/d = 5$, $L/d = 10$ and $L/d = 15$. When extrapolating the previous example ($\pm 1$ pixel), the percentage of variation increases as the number of pixels is smaller. Furthermore, the mm/pixel ratio is not constant since for a buckling length of $5d$, the camera has to be closer to the specimen to record more pixels, while for buckling lengths greater than $5d$, the camera has to move because the resolution of the camera does not allow

**Fig. 7** Examples of variations of ranges of values (*R*, *G*, *B*) for the same white mark.

$180 \leq R \leq 255$
$200 \leq G \leq 255$
$190 \leq B \leq 255$

$py_2 = 3178$

$200 \leq R \leq 255$
$200 \leq G \leq 255$
$190 \leq B \leq 255$

$py_2 = 3179$

$220 \leq R \leq 255$
$200 \leq G \leq 255$
$190 \leq B \leq 255$

$py_2 = 3181$



**Fig. 8** Examples of RGB filter variations classified by slenderness ratios using white marks.

(a) *L/d* = 5

$py_1 = 2235$
$py_2 = 2712$

$L = 477$

Assuming a difference of ±1 pixel:

$$\frac{\pm 1}{477} = \textbf{0,21\%}$$

(b) *L/d* = 10

$py_1 = 1961$
$py_2 = 2947$

$L = 986$

Assuming a difference of ±1 pixel:

$$\frac{\pm 1}{986} = \textbf{0,10\%}$$

(c) *L/d* = 15

$py_1 = 1762$
$py_2 = 3115$

$L = 1353$

Assuming a difference of ±1 pixel:

$$\frac{\pm 1}{1353} = \textbf{0,07\%}$$

to record the entire specimen in the photograph. For $L/d = 5$, the example in Fig. 8a has 477 pixels between $py_1$ and $py_2$, so assuming the difference in pixels, the variation is $\pm 1/477 = 0.21\%$. For $L/d = 10$ in Fig. 8b, the example has 986 pixels between $py_1$ and $py_2$, which implies that the variation is $\pm 1/986 = 0.10\%$. Finally, for

**Table 1** Mechanical properties of Grade 80 reinforcing bars.

| Reinforcement bar | $\phi 12$ |
|---|---|
| Yield stress $f_y$ (MPa) | 535.7 |
| Yield strain $\epsilon_y$ | 0.0028 |
| Modulus of elasticity $E_s$ (MPa) | 193059 |
| Ultimate stress $f_u$ (MPa) | 714.9 |
| Ultimate strain $\epsilon_u$ | 0.113 |

$L/d = 15$, the example in Fig. 8c has 1353 pixels between $py_1$ and $py_2$, so the variation is $\pm 1/1353 = 0.07\%$. In conclusion, all these photogrammetry problems may have an impact for those cases, where $L/d \leq 5$ and the total strain amplitude is lower than or equal to 0.02, since a variation of pixels of 0.21% for tests with small scales modifies the strain amplitude up to 50% allowed in this work. In those cases it is chosen not to use RGB filter, and only correct with the data obtained by the extensometer. Higher resolution cameras could fix this problem.
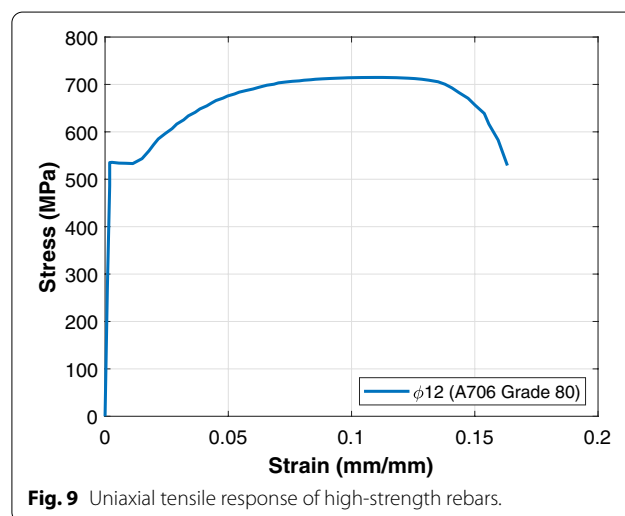
### 2.4 Tensile Test on High-Strength Rebar

The experimental procedure includes a first tensile test corrected by photogrammetry and summarized in Table 1 for a $\phi 12$ bar size, which serves as an evaluative test for estimate the mechanical parameters as references to be compared in the cyclic testing. The ratio of ultimate tensile strength to yield strength is 1.33, which is obtained using a yield strength established based on the 0.2% offset method. Irrespective of the method by which the yield strength is determined, the limit of 1.25 is the minimum specified $f_u/f_y$ ratio in ASTM A706 (2016) for ASTM A706 reinforcement.
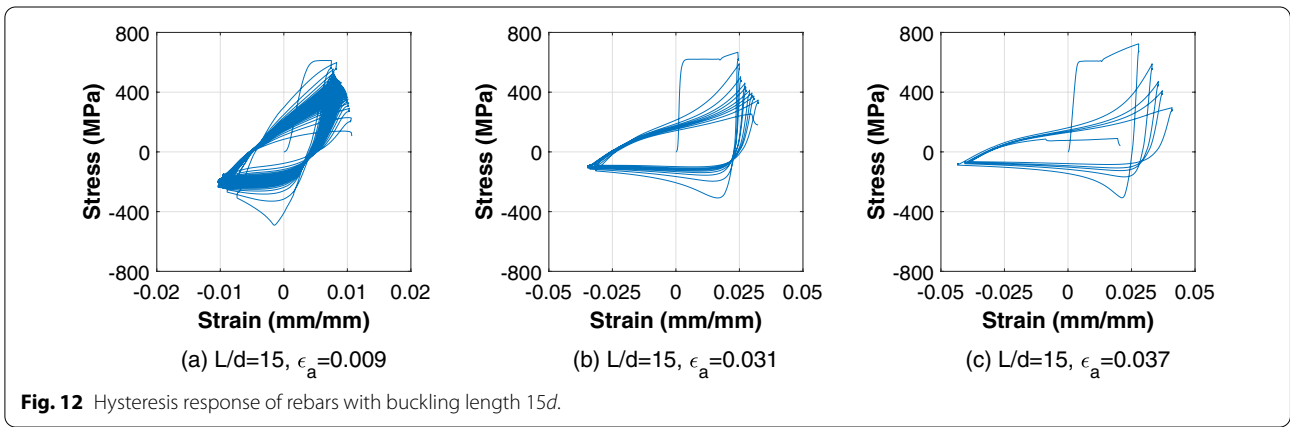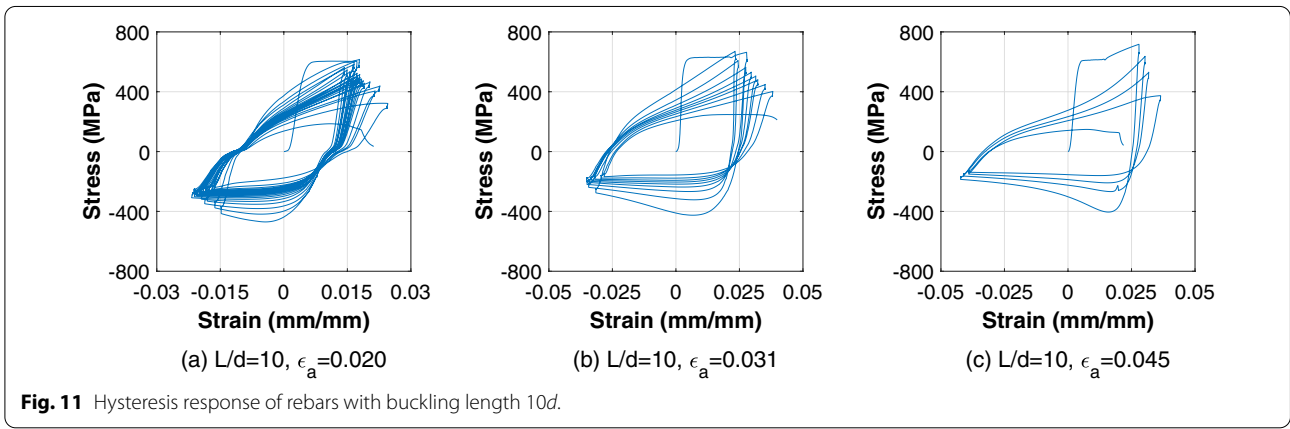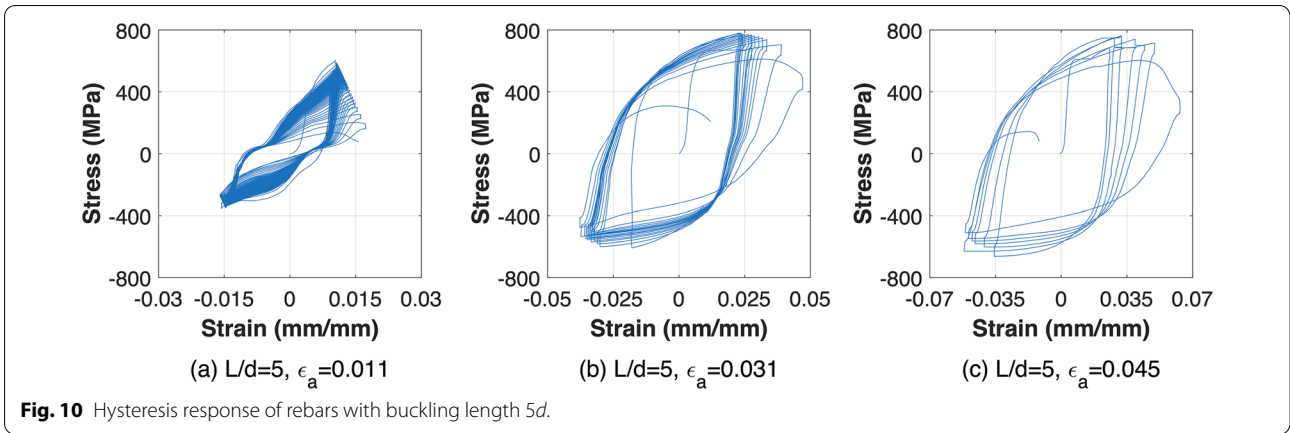
### 2.5 Fatigue Tests on High-Strength Rebars

This section provides the results from cyclic tests using photogrammetry. The results are analyzed and the total strain amplitude, number of half-cycles and dissipated energy until failure in the specimen are obtained. For cyclic testing, the experimental procedure also includes $\phi 12$ bar size. The buckling of high-strength reinforcement in RC members can span different slenderness ratios depending on the restraint offered by the transverse reinforcing bars, and they ratio values are chosen to characterize the global buckling length observed in damaged RC structures after the earthquake of 2010 in Chile as previously detailed. Therefore, the cyclic testing is performed on bars of multiple buckling lengths (ranging from 5$d$, 10$d$, and 15$d$) subjected to constant displacement amplitude loading with the total strain amplitude ranging from 0.01 to 0.05. The total length of steel bars ranges between 210 mm and 330 mm (depending on geometry, such as buckling length and diameter), inserting each specimen

over a length of 75 mm in each clamp. Altogether, photogrammetry is used to measure the axial strains experienced by specimens more accurately during the testing since reinforcement is prone to slippage or to experience plastic strain lengthening within the clamps. Cyclic loading continues until the specimen failure. Figs. 10, 11 and 12 illustrate the hysteresis response of Grade 80 reinforcing bars with multiple slenderness ratios including photogrammetry. The results show tensile properties similar to that presented in Table 1 and Fig.9, and an important reduction of compressive stress capacity due to buckling impact in the high-strength rebars. The hysteresis of the specimens for $L/d$=5 illustrated in Fig. 10 are symmetric in tensile and compression with less stress reduction excepting at the last cycle before failure; whereas, the reinforcing bars with $L/d$=10 in Fig. 11 and $L/d$=15 in Fig. 12 show unsymmetrical tensile–compression behavior with an important strength drop within the first cycle. Additionally, specimens with a greater slenderness ratio (i.e., higher than 5) show a reduction in energy dissipation with narrower cycles due to buckling observed as the force goes into compression as contrasted to the specimen with a lower slenderness ratio (generally near to 5) which exhibits wider hysteresis loops. In addition to this, buckling not only modifies the compression reaction of the specimens, but it also has damaging results on the tensile reaction in the following strain backtracks as exhibited in Figs. 10, 11 and 12. In the first peak-force phase, the strengths achieved by a specimen in the first cycle decrease considerably in the following cycles. The results obtained from the fatigue life tests on high-strength reinforcement are presented in Table 2.

Table 2 shows that Grade 80 reinforcing bars have variable fatigue life behaviors due to differences in their strain amplitudes and slenderness ratios. In general,



**Fig. 9** Uniaxial tensile response of high-strength rebars.

(a) L/d=5, $\epsilon_a$=0.011                          (b) L/d=5, $\epsilon_a$=0.031                          (c) L/d=5, $\epsilon_a$=0.045

**Fig. 10** Hysteresis response of rebars with buckling length 5*d*.



(a) L/d=10, $\epsilon_a$=0.020                        (b) L/d=10, $\epsilon_a$=0.031                        (c) L/d=10, $\epsilon_a$=0.045

**Fig. 11** Hysteresis response of rebars with buckling length 10*d*.



(a) L/d=15, $\epsilon_a$=0.009                        (b) L/d=15, $\epsilon_a$=0.031                        (c) L/d=15, $\epsilon_a$=0.037

**Fig. 12** Hysteresis response of rebars with buckling length 15*d*.

with a larger total strain amplitude higher than 0.02, the specimen consumes the total available energy of the steel faster, causing the reinforcing bar to fracture with fewer cycles. Also, the nominal strain amplitude and total strain amplitude corrected by photogrammetry remain uniform on average in all cases during the loading time.

The RGB methodology allows to reduce the total strain amplitude between 1.2% and 45.1%. In addition, the maximum transverse displacements $w_{max}$ obtained using Eq. 3 and shown in Table 2 that the value is numerically irrelevant, which means that the Eq. 1 can be considered as a suitable approximation for the buckling length. On

**Table 2** Summary results from low cycle fatigue tests on Grade 80 bars.

| Slenderness ratio $L/d$ | Young's modulus $E_s$ (MPa) | Nominal strain amplitude $\epsilon_{nom}$ | Total strain amplitude $\epsilon_a$ | Max. transverse displ. $w_{max}$ (mm) | Half-cycles to failure $2N_f$ | Total dissipated energy $W_{fT}$ (MPa) |
|---|---|---|---|---|---|---|
| 5 | 200013 | 0.020 | 0.011 | 4.2 | 246 | 1571 |
|  | 206458 | 0.035 | 0.031 | 7.1 | 34 | 826 |
|  | 201422 | 0.050 | 0.045 | 8.3 | 14 | 490 |
| 10 | 200579 | 0.021 | 0.020 | 11.8 | 42 | 292 |
|  | 208617 | 0.031 | 0.031 | 15.1 | 18 | 258 |
|  | 194772 | 0.051 | 0.045 | 15.9 | 8 | 140 |
| 15 | 206421 | 0.011 | 0.009 | 12.3 | 120 | 265 |
|  | 208828 | 0.031 | 0.031 | 21.3 | 18 | 158 |
|  | 207797 | 0.051 | 0.037 | 24.0 | 10 | 97 |

the other hand, at low slenderness ratios as illustrated in Fig. 10, there is an increase in the fatigue life behavior of the specimens as shown in Table 2, which is reduced with larger slenderness ratios as illustrated in Figs. 11 and 12. Furthermore, when the total strain amplitude is increased as shown in Table 2, all cycled rebars show shorter fatigue life since they achieve the plastic range earlier.

## 3 Calibrated Models for Low Cycle Fatigue

Achieved results from the low cycle fatigue tests on Grade 80 bars are analyzed and fatigue life calibrated models from literature are presented to relate the fatigue parameters (number of cycles to failure and total energy dissipated) with the total strain amplitude. The calibrated models developed and analyzed in previous studies are based on the total and plastic strain amplitudes, and based on hysteretic dissipated energy (Brown and Kunnath 2004; Koh and Stephens 1991; Mander et al. 1994). For this article, fitted models of fatigue life based on total strain amplitude are selected over the plastic strain amplitude due to the Bauschinger effect in reversal curves, which generates uncertainty in identifying accurately the plastic strain amplitude from the test data.

### 3.1 Fitted Model Based on the Total Strain Amplitude and Low Number of Half-Cycles

The original low cycle fatigue life of reinforcing bars can be represented and calibrated in terms of the total strain or plastic strain amplitude. The low cycle fatigue model presented by Koh and Stephens (1991) uses the total strain amplitude relating the number of half-cycles to failure and is defined as:

$$\epsilon_a = M(2N_f)^m, \tag{5}$$

where $\epsilon_a$ is the total strain amplitude on average experienced by the reinforcing bar, $M$ and $m$ are coefficients that can be fitted using the test data corrected by photogrammetry, and $N_f$ is the number of cycles until failure.

Fig. 13 shows the difference and variability of the number of half-cycles against the total strain amplitudes for high-strength reinforcement with multiple slenderness ratios. Fig. 13 exhibits the fatigue life curve decreases as the buckling length is increased for a constant diameter (i.e., as the specimens become more vulnerable to fracture). The results achieved from fatigue tests are calibrated to the power-law function on the results and a non-linear regression is performed to fit the coefficients for multiple buckling lengths considered. The low cycle fatigue life of high-strength reinforcement can be estimated employing Eq. 5, and the calibrated models based on half-cycles until failure are summarized in Table 3.

### 3.2 Fitted Model Based on the Total Strain Amplitude and Hysteretic Energy Dissipated

The hysteretic energy dissipated by the specimens subjected to uniform strain amplitude loading can be obtained by integrating the area enclosed under the stress–strain curve corrected by photogrammetry. The low cycle fatigue model proposed by Mander et al. (1994) relates the total strain amplitude $\epsilon_a$ with the total hysteretic energy dissipated until failure $W_{fT}$ and is represented as:

$$W_{fT} = W_a(\epsilon_a)^p, \tag{6}$$

where $W_a$ and $p$ are coefficients that can be fitted using the test results corrected by photogrammetry. Fig. 14

**Table 3** Calibrated models of low cycle fatigue based on total strain amplitude for multiple slenderness ratios.

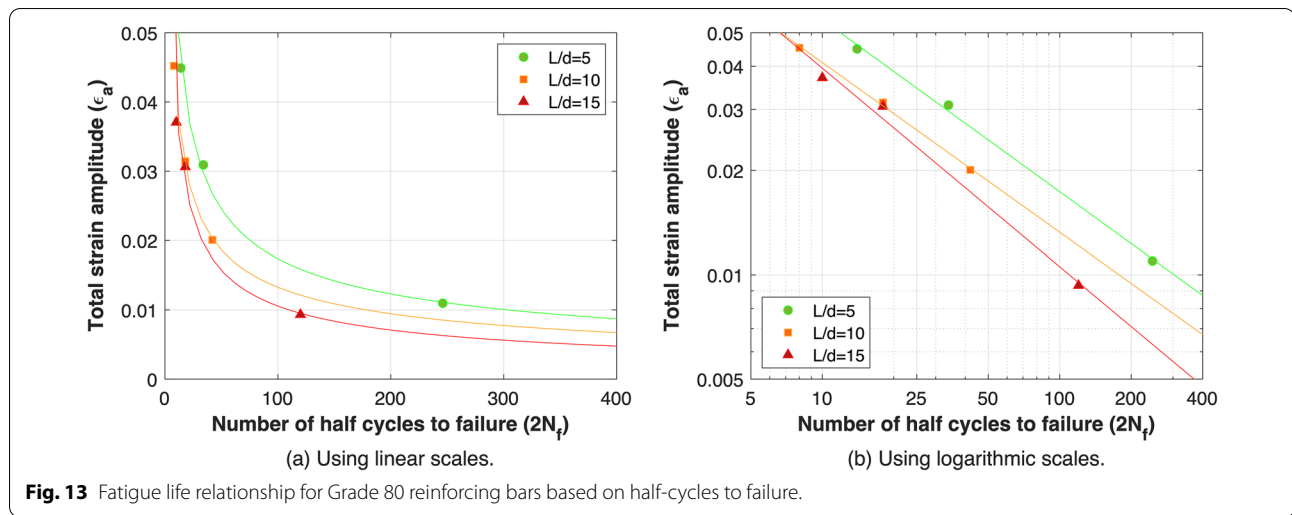| Reinforcement grade | Slenderness ratio $L/d$ | Equation | $R^2$ |
|---|---|---|---|
| 80 (550) | 5 | $\epsilon_a = 0.171(2N_f)^{-0.497}$ | 0.998 |
|  | 10 | $\epsilon_a = 0.127(2N_f)^{-0.490}$ | 0.998 |
|  | 15 | $\epsilon_a = 0.148(2N_f)^{-0.573}$ | 0.990 |

**Fig. 13** Fatigue life relationship for Grade 80 reinforcing bars based on half-cycles to failure.

shows the contrast of hysteresis energy dissipated for

**Table 4** Calibrated models of low cycle fatigue based on the total energy dissipated for multiple slenderness ratios.

| Reinforcement grade | Slenderness ratio $L/d$ | Equation | $R^2$ |
|---|---|---|---|
| 80 (550) | 5 | $\epsilon_a = 97.4(W_{fT})^{-1.225}$ | 0.959 |
| | 10 | $\epsilon_a = 4.89(W_{fT})^{-0.941}$ | 0.829 |
| | 15 | $\epsilon_a = 24.4(W_{fT})^{-1.383}$ | 0.863 |

high-strength reinforcement with multiple slenderness ratios. The results exhibited in Fig. 14 show that an increase in the slenderness ratio of a rebar can represent an important and meaningful reduction in the toughness dissipated due to early failure of the specimen. A calibrated fatigue model relating the quantity of cycled strain to fracture with the hysteretic energy dissipated is presented. The total energy dissipated to failure can be estimated using Eq. 6, and the coefficients are obtained for each buckling length by fitting the power–law function to the results, which are summarized in Table 4.

## 4 Conclusions

An experimental testing procedure to estimate the low cycle fatigue behavior of high-strength reinforcing bars Grade 80 under constant strain amplitude cyclic loading including photogrammetry by RGB methodology is presented. The main parameters considered in this research are the slenderness ratio (5, 10, and 15) and the total strain amplitude (0.01 to 0.05). In this article, the importance of photogrammetry is covered and the experimental results are analyzed. Additionally, a fatigue life model relating the total strain amplitude to the number

of cycles to failure and an energy-based fatigue performance model relating the total strain amplitude to the total energy dissipated are calibrated. The main conclusions that can be detailed from the results are:

1. The use of photogrammetry by RGB methodology provides greater data accuracy compared to the strains provided by only traditional displacement sensors when lateral support spacing are larger than $5d$ with total strain amplitude higher than 0.02, since this methodology detects more information from the measurement, such as strain penetration or rotations in embedments. However, for buckling length shorter than or equal to $5d$ and total strain amplitude lower than or equal to 0.02, the RGB filter is not considered due to the ratio of pixels with the real distance, which can generate important variations in the total strain amplitude. Better camera quality or closeness to the specimen would revert the shortcoming.

2. Inelastic buckling described and observed of high-strength reinforcing bars results in considerable loss of its compressive and tensile carrying capacity. In addition to negatively impacting the fatigue performance of the rebar, buckling also affects its overall hysteretic behavior. Despite this, ASTM A706 Grade 80 meets the requirement that the tensile-to-yield strength ratio exceeds 1.25, which is frequently established by US design codes for reinforcement used in seismic applications.

3. When high-strength reinforcing bars are cycled with buckling lengths shorter or equal than $5d$, specimens are tested and damaged to failure through a larger number of cycles; whereas, for high-strength reinforcing bars with lateral support length longer than $5d$, fatigue fracture occurs at lower numbers of

**Fig. 14** Fatigue life relationship for Grade 80 reinforcing bars based on total energy dissipated.

cycles. An increase in the slenderness ratio results in a meaningful reduction in their fatigue performance since it makes them more prone to buckling and fracturing.

4. The previous discussion illustrates that when the total strain amplitude is increased, all cycled high-strength reinforcing bars show shorter fatigue performance since the specimens achieve the plastic range and available energy faster, implying that the fatigue failure will occur earlier. Decreasing the transverse reinforcement spacing for longitudinal high-strength rebars can reduce their buckling and significantly enhance its fatigue behavior.

## Declarations

### Competing interests
The authors declare that they have no competing interests.

### Author information
Jorge Egger Roa, Civil Engineer, Department of Civil Engineering, University of Chile, Santiago, Chile. Fabian Rojas Barrales, Assistant Professor, Department of Civil Engineering, University of Chile, Santiago, Chile. Leonardo Massone Sánchez, Associate Professor, Department of Civil Engineering, University of Chile, Santiago, Chile.

### References
AASHTO. (2017). *LRFD Bridge Design Specifications* (8th ed.). Washington, DC: American Association of State Highway and Transportation Officials.
ACI. (2019). *Building Code Requirements for Structural Concrete (ACI 318–19) and Commentary (ACI 318R–19)*. Farmington Hills, MI: American Concrete Institute.
ASTM. (2016). *Standard Specification for Deformed and Plain Low-Alloy Steel Bars for Concrete Reinforcement, ASTM A706/A706M-16*. West Conshohocken, PA: ASTM International.
Barbosa, A., Trejo, D., Nielson, D., Mazerei, V. & Tibbits, C. (2017). High strength reinforcing steel bars: Low cycle fatigue behavior (Final Report - Part B). Oregon Department of Transportation. https://rosap.ntl.bts.gov/view/dot/32013
Blaber, J., Adair, B., & Antoniou, A. (2015). Ncorr: Open-Source 2D Digital Image Correlation Matlab Software. *Experimental Mechanics, 55,* 1105–1122. https://doi.org/10.1007/s11340-015-0009-1.
Brown, J., & Kunnath, S. (2004). Low-Cycle fatigue failure of reinforcing steel bars. *ACI Materials Journal, 101*(6), 457–466. https://doi.org/10.14359/13484.
Carpenter, L., Naeim, F., Lew, M., Youssef, N., Rojas, F., Saragoni, R., & Schachter, M. (2011). Performance of tall buildings in Viña del Mar in the 27 February 2010 offshore Maule, Chile earthquake. *The Structural Design of Tall and Special Buildings, 20,* 17–36. https://doi.org/10.1002/tal.672.
DSLR Remote Pro (2017). Multi-Camera, version 1.9.5, reeze Systems Limited, Camberley, UK.
Elistratkin, M. Y., Lesovik, V. S., Zagorodnjuk, L. H., Pospelova, E. A., & Shatalova, S. V. (2018). IOP Conf. Series: New point of view on materials development. *Materials Science and Engineering, 327,* 032020. https://doi.org/10.1088/1757-899X/327/3/032020.
Fisher, J., Kulak, G., & Smith, I. (1998). A Fatigue Primer for Structural Engineers. National Steel Bridge Alliance, American Institute of Steel Construction. https://www.aisc.org/globalassets/nsba/technical-documents/a-fatigure-primer-for-structural-engineers.pdf.

Ghannoum, W., & Slavin, C. (2016). Low-cycle fatigue performance of high-strength steel reinforcing bars. *ACI Materials Journal, 113*(6), 803–814. https://doi.org/10.14359/51689116.

Hu, M., Han, Q., Xu, K., & Du, X. (2019). Impact of corrosion on cyclic behaviors of ultra-high-strength reinforcing bars. *Construction and Building Materials, 209,* 606–618. https://doi.org/10.1016/j.conbuildmat.2019.03.182.

Koh, S., & Stephens, R. (1991). Mean stress effects on low cycle fatigue for a high strength steel. *Fatigue & Fracture of Engineering Materials & Structures, 14*(4), 413–428. https://doi.org/10.1111/j.1460-2695.1991.tb00672.x.

López, J. (2019). Technical feasibility study of the use of welded reinforcing steel for reinforced concrete. Civil Engineer Thesis, Department of Civil Engineering, Faculty of Physical Sciences and Mathematics, University of Chile. http://repositorio.uchile.cl/handle/2250/170979

Mander, J., Panthaki, F., & Kasalanti, A. (1994). Low-cycle fatigue behaviour of reinforcing steel. *Journal of Materials in Civil Engineering ASCE, 6*(4), 453–468. https://doi.org/10.1061/(ASCE)0899-1561(1994)6:4(453).

Massone, L. (2013). Fundamental principles of the reinforced concrete design code changes in Chile following the Mw 8.8 earthquake in 2010. *Engineering Structures, 56*, 1335–1345. https://doi.org/10.1016/j.engstruct.2013.07.013

Massone, L., & Herrera, P. (2019). Experimental study of the residual fatigue life of reinforcement bars damaged by an earthquake. *Materials and Structures, 52,* 61. https://doi.org/10.1617/s11527-019-1361-x.

MATLAB (2018). R2018b, The MathWorks Inc., Natick, Massachusetts.

Naeim, F., Lew, M., Carpenter, L., Youssef, N., Rojas, F., Saragoni, R., & Schachter, M. (2011). Performance of tall buildings in Santiago, Chile during the 27 February 2010 offshore Maule, Chile earthquake. *The Structural Design of Tall and Special Buildings, 20,* 1–16. https://doi.org/10.1002/tal.675.

NCh204. (2020). *Acero - Barras laminadas en caliente para hormigón armado (Steel - Hot rolled bars for reinforced concrete)*. Chile: Instituto Nacional de Normalización - INN.

Pan, B., Qian, K., Xie, H., & Asundi, A. (2009). Two-dimensional digital image correlation for in-plane displacement and strain measurement: a review. *Measurement Science and Technology, 20*(6), 062001. https://doi.org/10.1088/0957-0233/20/6/062001.

Rojas, F., Lew, M., & Naeim, F. (2010). An overview of building codes and standards in Chile at the time of the 27 February 2010 offshore Maule, Chile earthquake. *The Structural Design of Tall and Special Buildings, 19,* 853–865. https://doi.org/10.1002/tal.676.

Rojas, F., Naeim, F., Lew, Marshall, Carpenter, L., Youssef, N., Saragoni, R., & Schachter, M. (2011). Performance of tall buildings in Concepción during the 27 February 2010 moment magnitude 8.8 offshore Maule, Chile earthquake. *The Structural Design of Tall and Special Buildings, 20,* 37–64. https://doi.org/10.1002/tal.674.

Selek, M. (2016). A New Autofocusing Method Based on Brightness and Contrast for Color Cameras. *Advances in Electrical and Computer Engineering, 16*(4), 39–44. https://doi.org/10.4316/AECE.2016.04006

Sokoli, D., Shekarch, W., Buenrostro, E., & Ghannoum, W. (2014). Advancing behavioral understanding and damage evaluation of concrete members using high-resolution digital image correlation data. *Earthquakes and Structures, 7*(5), 609–626. https://doi.org/10.12989/eas.2014.7.5.609.

Sokoli, D., Hogsett, G., Limantono, A., Suselo, A., Al-Tarafany, D., Rodgers, S., & Ghannoum, W. (2019). Acceptable Elongations and Low-Cycle Fatigue Performance for High-Strength Reinforcing Bars (Final Report). The University of Texas at San Antonio, Charles Pankow Foundation. https://www.pankowfoundation.org/s/2019-08-CPF-Final-Report.pdf

Tripathi, M., Dhakal, R., Dashti, F., & Massone, L. (2018). Low-cycle fatigue behaviour of reinforcing bars including the effect of inelastic buckling. *Construction and Building Materials, 190,* 1226–1235. https://doi.org/10.1016/j.conbuildmat.2018.09.192.

Wallace, J., Massone, L., Bonelli, P., Dragovich, J., Lagos, R., Lüders, C., & Moehle, J. (2012). Damage and Implications for Seismic Design of RC Structural Wall Buildings. *Earthquake Spectra, 28*(S1), S281–S299. https://doi.org/10.1193/1.4000047.

Wang, G., Ma, Y., Wang, L., & Zhang, J. (2021). Experimental study and residual fatigue life assessment of corroded high-tensile steel wires using 3D scanning technology. *Engineering Failure Analysis, 124,* 105335. https://doi.org/10.1016/j.engfailanal.2021.105335.

Yang, H., Wu, Y., Pengcheng, M., & Chen, J. (2016). Improved Nonlinear Cyclic Stress-Strain Model for Reinforcing Bars Including Buckling Effect and Experimental Verification. *International Journal of Structural Stability and Dynamics, 16*(1), 1640005. https://doi.org/10.1142/S0219455416400058.

## Publisher's Note